KRONOS FUSION ENERGY

PAPER 2.102 · THE KRONOS 2026 SERIES

Balance of Plant for a Compact Spherical-Tokamak Breeder: Heat Rejection, Cryoplant Load-Balancing, and Vacuum Scheduling for the 16.84 T Cold Mass

Between a fusion core and the grid sits the balance of plant (BOP), and beneath the whole machine sit the cryogenic and vacuum services that keep the cold mass superconducting and...

Read it live — 3-D model · physics validator · film series

BY P I FORD, R J WEGGEL AND C WEGGEL

2026 · EDITORIAL EDITION

THE OFFICIAL RECORD

What this document is, and how to read its numbers

This is a combined editorial. It gathers, in one volume, the two design studies Kronos Fusion Energy released in 2026 — a compact spherical-tokamak tritium/helium-3 breeder and a deuterium–helium-3 tandem-mirror generator — together with the intellectual-property estate, the people, and, in the internal edition, the full commercial case. The scientific text is the same text that appears in the arXiv preprints and the journal submissions; the editorial adds the apparatus a reader needs to hold the whole program at once, and nothing in the physics is altered to fit it.

THE HONESTY STANCE IS THE ASSET

Every headline quantity carries an **evidence class** — DERIVED RECOMPUTED MEASURED REQUIREMENT — and, where a number is a modelled extrapolation rather than a demonstrated value, it is labelled as such and its downside is shown next to it. Several quantities in the underlying corpus moved after first publication; where a value has been withdrawn or restated, the record says so plainly. This is deliberate: a diligence team will find the load-bearing assumptions, so the document surfaces them first.

TWO EDITIONS

This volume is issued in two editions. The **public edition** (light) carries the physics and the design only — no dollar, price, or per-kilogram figure appears anywhere in it. The **internal edition** (dark) adds the economics, the funding architecture, and the defense-commercial analysis, and is marked *Confidential* accordingly; it is not for public distribution. Where the commercial case rests on a modelled assumption rather than a demonstrated one, it is labelled as such and its downside is shown alongside it, on the same terms as the physics.

TITLE	The Kronos Fleet — Hyperion · Aegis · MetroVolt: A Combined Design & Commercialization Study
AUTHOR	Priyanca Ford, Founder & CEO, on behalf of Kronos Fusion Energy
EDITION	2026 Combined Editorial · first issue
COMPANION WORKS	The five-paper arXiv drop — (1) Breeder, (2) Burner, (3) REBCO magnet & tape, (4) Direct Energy Conversion, (5) AI/ML/Quantum control — with matching numbered Zenodo deposits, plus the IOP journal and IAEA-FEC submissions. Patents were filed before the drop.
NAMING	Hyperion = the breeder; Aegis (defense) and MetroVolt (data-center) = one generator in two housings. Internal mode letters (D1, L) do not appear on public surfaces.
STATUS	Conceptual design & simulation study. Nothing herein is a construction commitment.

HOW TO READ THIS VOLUME

The fleet at a glance, and the way its numbers are marked

This volume opens with *Orientation*, presents the five research papers as a bound sequence, and closes with the *Apparatus*. *Foundations* sets out the three general results both machines rest on. *Paper One* is the Hyperion breeder; *Paper Two* the Aegis / MetroVolt generator; *Papers Three, Four and Five* are the enabling science — high-field REBCO magnets and tape, direct energy conversion, and the AI / ML / quantum control stack. A *Digital Twin & 3-D Model* part follows, then the *Environmental* profile. The *Economics* and levelized cost and the *Business Case* and diligence record appear in the internal edition only; the *Simulations* proof record and the Apparatus — patent portfolio, team, limitations, and sources — close both editions.

THE FLEET AT A GLANCE

	HYPERION	AEGIS	METROVOLT
Role	Strategic-isotope foundry	Defense installation power	Campus power
Machine	**Spherical tokamak**	**Tandem mirror**	**Tandem mirror**
Fuel	Deuterium–tritium	Deuterium–helium-3	Deuterium–helium-3
Delivers	Tritium · ^{3}He · 14 MeV n	Resilient installation power	Firm campus power
Physics bar	**Fusion gain only**	Closure (gates named)	Closure + lunar ^{3}He
In the fleet	Breeds the fuel	Proves the generator	Commercial destination

HOW THE NUMBERS ARE MARKED

Every headline quantity carries an evidence class — DERIVED from first principles, RECOMPUTED from raw data, MEASURED in hardware, or a REQUIREMENT yet to be met. Financial figures carry a case label and are confined to the internal (confidential) edition. Values that moved after first publication are shown as withdrawn or restated rather than quietly changed. A capability you can evaluate is one whose limits are on the page.

ABSTRACT

Balance of Plant for a Compact Spherical-Tokamak Breeder: Heat Rejection, Cryoplant Load-Balancing, and Vacuum Scheduling for the 16.84 T Cold Mass

Between a fusion core and the grid sits the balance of plant (BOP), and beneath the whole machine sit the cryogenic and vacuum services that keep the cold mass superconducting and the chamber evacuated. We formalise the BOP of the Kronos Hyperion breeder as a coupled thermal–fluid–cryogenic–vacuum system and reduce it to a set of governing equations, a numerical formulation, and a demonstrated design envelope. At the ratified design point ($Q = 3.076$, $P_{\mathrm{fus}} = 85.04\,MW$, $I_p = 9.66\,MA$, $\delta = -0.30$, $B_0 = 8\,T$, $\kappa = 2.0$, $R_0 = 1.20\,m$, aspect ratio $A = 2.5$) the blanket dissipates a thermal power $P_{\mathrm{th}} = M_n P_n + P_{\mathrm{chg}} = 95.2\,MW$ built from a neutron power $P_n = 67.79\,MW$ (energy multiplication $M_n = 1.15$) and a charged-particle power $P_{\mathrm{chg}} = 17.25\,MW$; removing it with helium at a temperature rise $\Delta T = 200\,K$ requires a mass flow $\dot{m} = P_{\mathrm{th}}/(c_p \Delta T) = 91.7\,kg/s$, a volumetric flow of $\approx 14.8\,m^3/s$ at the inlet loop condition ($8\,MPa$, 350 °C). The decisive BOP result is passive safety: after shutdown the decay heat falls as $P_d(t) \propto t^{-0.203}$ from $\approx 0.95\,MW$ at 1 s to $\approx 95\,kW$ at one day, and a Stefan–Boltzmann balance over the compact plasma-facing area ($\approx 36\,m^2$, emissivity 0.5) rejects those levels at equilibrium wall temperatures of $\approx 711\,^\circ C$ and $\approx 290\,^\circ C$ respectively — below steel-damage territory, with no forced cooling required for survival; a lumped-capacitance transient shows the realised peak lies far below the quasi-static bound. The cryogenic envelope is set by two *distinct* magnets: the breeder centrepost at $16.84\,T$ (temperature margin 49.5 K, load fraction 0.27) and the burner plug coil at $26.49\,T$ (margin 37.1 K, load fraction 0.43); we write the $4.5\,K$ refrigeration penalty (≈ 219 W of input per W lifted at 30% Carnot) and cast cryoplant load-balancing as a constrained optimisation. Vacuum scheduling follows a pump-down ordinary differential equation to an outgassing-limited base of $\sim 1e-7\,Pa$. Power conversion runs by two routes — a breeder thermal cycle from the $95.2\,MW$ blanket and burner direct energy conversion at plant efficiency 0.49 (module 0.70). On this demonstrated envelope we define a cryo-vacuum control backbone — load-balancer, refrigeration-COP optimiser, vacuum scheduler and heat-exchanger fouling monitor — each gated by a single testable criterion. Every quantitative claim traces to a frozen entry in the Kronos Physics De-Risking Register.

Open-access deposit (code & data, CC BY 4.0): DOI 10.5281/zenodo.22645901 · Zenodo community *kronos_fusion_energy*. Explore it live: interactive 3-D model · physics validator.

Keywords: balance of plant · heat rejection · passive decay heat · cryogenics · load-balancing · vacuum scheduling · direct energy conversion · spherical-tokamak breeder

CONTENTS

Table of Contents

NOMENCLATURE

Symbols, units, and the names of things

Q	plasma (fusion) gain, P_{fus}/P_{aux}
Q_E	engineering gain, net electric out / recirculating in
H_{98}	confinement enhancement over the IPB98(y,2) scaling
Z_{eff}	effective ion charge
c_{ee}	electron–electron bremsstrahlung leading coefficient, 2.120022 (exact)
τ_E	energy confinement time
I_p	plasma current
R_0, a	major radius, minor radius
κ, δ	elongation, triangularity
β_N	normalized plasma beta (Troyon-normalized)
TBR	tritium breeding ratio
DEC	direct energy conversion
CF	plant capacity factor (availability)
FOAK / NOAK / BOAK	first / n^{th} / best of a kind
Hyperion	the ST breeder (internal: Mode D2)
Aegis	the generator, defense/installation housing (internal: Mode M)
MetroVolt	the generator, data-center housing (Mode M)

balance of plant; heat rejection; passive decay heat; cryogenics; load-balancing; vacuum scheduling; direct energy conversion; spherical-tokamak breeder

§ 1

Introduction

WHY THE BALANCE OF PLANT IS THE LOAD-BEARING ENGINEERING PROBLEM

A fusion core produces power only in the abstract until the balance of plant (BOP) around it removes the heat, converts it, and holds the machine in its operating state. For a compact, high-power-density spherical tokamak (ST) this is not a downstream afterthought: the same compactness that makes the ST an attractive neutron source and breeder platform [1,2] concentrates the heat flux, shortens the thermal-transient timescales, and drives the magnets to fields where the cryogenic margin is a first-order design variable. The BOP therefore sets three coupled envelopes that any credible compact-breeder design must meet simultaneously: (i) a *thermal* envelope — a coolant path that removes the blanket heat with adequate margin; (ii) a *safety* envelope — a demonstrable route to reject post-shutdown decay heat without relying on forced cooling; and (iii) a *cryo-vacuum* envelope — a refrigeration and pumping plant that holds the superconducting cold mass and the vessel base pressure across the full range of operating loads.

This paper establishes those three envelopes for the Kronos Hyperion breeder as a set of governing equations, gives a numerical formulation and convergence study, reports the demonstrated design point produced on the NVIDIA GPU high-performance-computing (HPC) campaign, and defines the cryo-vacuum control backbone built to the demonstrated envelope. The single result that most changes the engineering conversation is a *passive* one: at $\approx 95\,MW$ of blanket thermal power the machine can shed its decay heat by radiation and conduction alone, at structure temperatures below the damage threshold. Passive rejection removes forced post-shutdown cooling from the list of survival-critical systems and, with it, an entire branch of the classical fission-derived loss-of-coolant accident tree.

PRIOR ART

The engineering of fusion power plants is a mature literature. The European DEMO programme has produced successive integrated designs of the primary heat-transport system, blanket and BOP [4,5], with the helium-cooled pebble-bed (HCPB) blanket a canonical high-pressure helium concept [6]. The tritium fuel cycle and the blanket conditions required for self-sufficiency are set out by Abdou *et al.* [7]. Post-shutdown decay heat and the activation inventory that produces it are computed for DEMO-class machines with modern activation transport [8] using inventory codes such as FISPACT-II [9] coupled to Monte-Carlo neutron transport (OpenMC [10]). The cryogenic side draws on large-scale helium refrigeration for accelerators and tokamaks [12] and on high-temperature superconductor (HTS) current leads that minimise the room-temperature-to-cold-mass heat leak [13]; the torus vacuum and its cryopumps are analysed with rarefied-gas methods [14]. Power conversion divides into thermal cycles for neutron-dominated machines and direct energy conversion (DEC) for the charged-particle output of advanced-fuel mirrors, a line running from Post's mirror programme [16] through the Barr–Moir beam direct converter [15]. The magnet cold mass itself is a no-insulation (NI) REBCO winding of the class behind recent record fields [17,18], whose quench behaviour and protection have their own literature [19,20].

What is missing for a *compact nuclear ST* is a single, internally consistent BOP treatment that (a) closes the thermal balance at the ratified operating point rather than a generic one, (b) proves the passive decay-heat case with an explicit transient model, (c) correctly separates the two distinct high-field magnets that set the cryogenic load, and (d) hands a real-time control backbone a demonstrated envelope with testable acceptance gates. This paper contributes exactly that. Complementary Kronos studies treat the cold-mass thermal budget and the $4.5\,K$ refrigeration plant in detail [C1], the blanket and divertor thermal-hydraulics and the walk-away safety case [C2], the consumable centrepost and magnet integrity [C3], the four coupled digital twins that host the control backbone [C4], the burner direct-energy converter [C5], the $26.49\,T$ plug coil [C6], and the vacuum-vessel structural mechanics [C7]; the present paper is the BOP synthesis that ties their envelopes together.

CONTRIBUTION AND ORGANISATION

We give: a formal statement of the BOP as a coupled system and its boundary quantities (§2); the governing equations for the primary heat-transport loop, the passive decay-heat transient, the cryogenic refrigeration thermodynamics with a load-balancing optimisation, the vacuum pump-down, and the two conversion routes (§3); the GPU-HPC computational methodology that produced the results (§4); the numerical formulation and a convergence study for the stiff radiative transient (§5); the results with eleven figures and supporting tables (§6); a quantitative comparison against published DEMO/ITER numbers (§7); one honest limitation (§8); and the conclusion (§9). Every number traces to a frozen result in the Kronos Physics De-Risking Register [31]; serial identifiers (e.g.\ BR-L1-A9) are given inline so each is auditable.

§ 2

The balance-of-plant system and its boundary quantities

The BOP is organised as a *power path* in series with a set of *services* that are coupled to it (figure 1). The power path carries fusion power from the plasma into the breeding blanket, through the primary helium loop, and into power conversion; the services — the cryoplant, the vacuum system, and the passive heat-rejection path — hold the operating state and are coupled to the power path through a small set of interface quantities. Writing the plant sub-states as a thermal-fluid state x_H (loop temperatures, pressures, flows), a cryogenic state x_C (cold-mass temperatures, refrigeration load), and a vacuum state x_V (chamber pressure, throughput), the dominant couplings are

$$\begin{aligned} \text{blanket} \to \text{loop:} &\quad P_{\text{th}} \longmapsto \{\dot{m},\ \Delta T\}, \\ \text{structure} \to \text{cryoplant:} &\quad T_{\text{struct}},\ \dot{Q}_{\text{nuc}} \longmapsto \dot{Q}_{\text{cryo}}, \\ \text{chamber} \to \text{vacuum:} &\quad Q_{\text{out}}(t) \longmapsto p_{\text{vac}}, \\ \text{loop} \to \text{conversion:} &\quad \{T_{\text{out}}, \dot{m}\} \longmapsto P_{\text{elec}}. \end{aligned}$$

Each service evolves under its own dynamics driven by its actuators u and by the coupling inputs from the power path,

$$\frac{\mathrm{d}\ x_s}{\mathrm{d}t} = f_s(\ x_s,\ u_s,\ c_s), \qquad s \in \{H, C, V\},$$

and the BOP acceptance condition is that all cryogenic and vacuum setpoints are held while the plant heat-and-power balance closes to tolerance. The remainder of the paper makes each of equations (1)–(1) concrete.

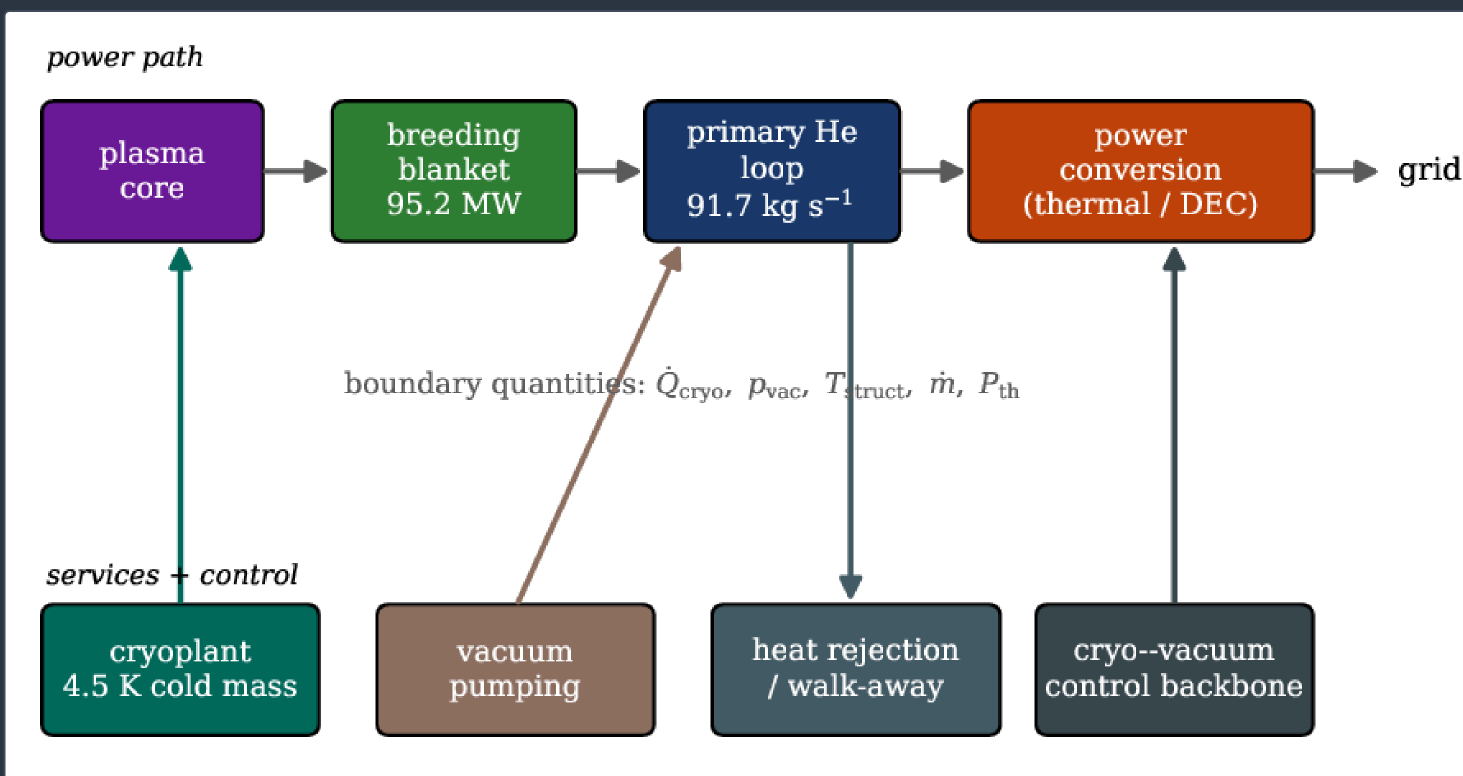

(Schematic.) The balance-of-plant system: a power path (plasma → blanket → primary helium loop → power conversion) in series with the services (cryoplant, vacuum, passive heat rejection) and the cryo-vacuum control backbone. Directed edges carry the boundary quantities of equations (1)–(1); no data values are encoded, the figure shows structure only.

§ 3

Governing equations and formal problem

PRIMARY HEAT-TRANSPORT LOOP

Power split and coolant duty. At the ratified design point (BR-L1-A9) the fusion power $P_{\text{fus}} = 85.04\,MW$ divides into a neutron power $P_n = 67.79\,MW$ and a charged-particle power $P_{\text{chg}} = 17.25\,MW$. Neutrons deposit their energy volumetrically in the breeding blanket, where exothermic ^{6}Li and ^{9}Be reactions multiply the nuclear heating by an energy-multiplication factor M_n typical of Li/Be-bearing blankets [6]. The blanket thermal power is therefore

$$P_{\text{th}} = M_n\,P_n + P_{\text{chg}}, \qquad M_n = 1.15, \qquad P_{\text{th}} = 95.2\,\text{MW}.$$

A single-phase coolant of specific heat c_p raised through a temperature rise ΔT carries this power at a mass flow set by the steady energy balance $P_{\text{th}} = \dot{m}\,c_p\,\Delta T$, hence

$$\dot{m} = \frac{P_{\text{th}}}{c_p\,\Delta T} = \frac{95.2\,\text{MW}}{(5193\,\text{J/kgK})(200\,\text{K})} = 91.7\,\text{kg/s},$$

for helium at $c_p = 5193\,J/kgK$ over the loop range §Irange350550 at 8 MPa. Treating helium as ideal with specific gas constant $R_{\text{He}} = 2077\,J/kgK$, the inlet density is $\rho_{\text{in}} = p/(R_{\text{He}}T_{\text{in}}) = 6.19\,kg/m^3$ and the inlet volumetric flow is $\dot{V}_{\text{in}} = \dot{m}/\rho_{\text{in}} \approx 14.8\,m^3/s$, which sets the header and circulator sizing.

Convective heat transfer. Heat crosses from the structure into the coolant through a forced-convection film. For fully developed turbulent flow in the blanket channels the Nusselt number follows the Dittus–Boelter correlation [26,27],

$$Nu = \frac{h\,d_h}{k} = 0.023\,Re^{0.8}\,Pr^{0.4}, \qquad Re = \frac{\rho\,\bar{u}\,d_h}{\mu},$$

with h the film coefficient, d_h the hydraulic diameter, k, μ, Pr the coolant conductivity, viscosity and Prandtl number, and $\bar{u}$ the mean channel velocity. Equation (5) fixes the wall-to-coolant temperature drop $\Delta T_{\text{film}} = q''/h$ for a given surface heat flux q'' and so, together with (3), closes the peak-temperature margin of the first wall and blanket structure.

Pumping power. The circulator must overcome the loop pressure drop Δp, dominated by friction in the blanket channels,

$$\Delta p = f\,\frac{L}{d_h}\,\frac{\rho\,\bar{u}^2}{2}, \qquad P_{\text{pump}} = \frac{\dot{V}\,\Delta p}{\eta_c} = \frac{\dot{m}\,\Delta p}{\rho\,\eta_c},$$

with Darcy friction factor f, channel length L, and circulator efficiency η_c. Because P_{pump} scales as $\dot{m}^3/\rho^2$ at fixed geometry, high pressure and a large ΔT are both levers that keep the pumping fraction $P_{\text{pump}}/P_{\text{th}}$ small; at the design point a representative $\Delta p \sim 0.3\,MPa$ and $\eta_c = 0.8$ give a pumping fraction of a few percent (§6).

PASSIVE WALK-AWAY DECAY HEAT

Decay-heat law. After shutdown the neutron source vanishes but the activated structure continues to release decay heat. The two frozen anchors (BR-L1-A9) are $P_d(1\,s) \approx 0.95\,MW$ and $P_d(1\,) \approx 95\,kW$. A single power law through these anchors,

$$P_d(t) = P_d(t_0)\left(\frac{t}{t_0}\right)^{-\alpha}, \qquad \alpha = \frac{\ln\left[P_d(t_0)/P_d(t_1)\right]}{\ln(t_1/t_0)} = \frac{\ln 10}{\ln 86400} = 0.203,$$

captures the order-of-magnitude fall over the first day and is the BOP-level surrogate for a full activation inventory (the honest refinement of §8). The exponent $\alpha \approx 0.20$ is characteristic of an activation-dominated fusion structure [8].

Radiative rejection. The compact plasma-facing structure of area A and emissivity ε radiates to surroundings at T_{amb}. Equating the decay heat to the net radiative loss gives the quasi-static equilibrium wall temperature,

$$P_d(t) = \varepsilon\,\sigma\,A\left(T_{\text{eq}}^4 - T_{\text{amb}}^4\right) \implies T_{\text{eq}}(t) = \left[\frac{P_d(t)}{\varepsilon\,\sigma\,A} + T_{\text{amb}}^4\right]^{1/4},$$

with σ the Stefan–Boltzmann constant. For $A = 36\,m^2$ (the compact plasma-facing area only, a conservative choice), $\varepsilon = 0.5$ and $T_{\text{amb}} = 300\,K$, equation (8) gives $T_{\text{eq}}(1\,s) \approx 984\,K$ ($\approx 711\,^\circ C$) and $T_{\text{eq}}(1\,) \approx 564\,K$ ($\approx 290\,^\circ C$; $\approx 280\,^\circ C$ for radiation to cold surroundings). Both sit below steel structural-damage territory, so the required equilibrium temperature never enters the failure regime.

Loss-of-forced-cooling transient. The realised temperature is bounded above by (8) because the structure has finite thermal mass. Lumping the structure into a heat capacity mC, the loss-of-forced-cooling (LOFC) transient obeys

$$mC\,\frac{\mathrm{d}T}{\mathrm{d}t} = P_d(t) - \varepsilon\,\sigma\,A\left(T^4 - T_{\text{amb}}^4\right), \qquad T(0) = T_{\text{amb}}.$$

Equation (9) is the nonlinear ordinary differential equation (ODE) whose numerical solution is the central safety result: with a representative $mC = 1e7\,J/K$ the trajectory peaks far below the zero-thermal-mass bound of (8) and then tracks the decaying source downward, so the machine survives a complete loss of forced cooling on radiation and conduction alone.

CRYOGENIC REFRIGERATION THERMODYNAMICS

Refrigeration penalty. Holding the cold mass at T_c against a heat load $\dot{Q}_{\text{cryo}}$ costs input power bounded below by the Carnot work of a refrigerator operating between T_c and the rejection temperature T_h,

$$\mathrm{COP}_{\text{Carnot}} = \frac{T_c}{T_h - T_c}, \qquad P_{\text{in}} = \frac{\dot{Q}_{\text{cryo}}}{\eta_{\text{plant}}\,\mathrm{COP}_{\text{Carnot}}} = \frac{\dot{Q}_{\text{cryo}}}{\eta_{\text{plant}}}\,\frac{T_h - T_c}{T_c},$$

where η_{plant} is the fraction of Carnot achieved by a real helium plant (large plants reach $\eta_{\text{plant}} \approx 0.3$ [12]). At $T_c = 4.5\,K$ and $T_h = 300\,K$ the ideal specific power is $(T_h - T_c)/T_c \approx 65.7\ \mathrm{W\,W^{-1}}$ and the plant specific power is $\approx 219\ \mathrm{W\,W^{-1}}$: every watt deposited in the cold mass costs of order 200 W at the wall, which is why minimising $\dot{Q}_{\text{cryo}}$ is the governing cryogenic design objective.

Cold-mass load budget. The cryogenic load is the sum of a static part (conduction down the supports and current leads, thermal radiation from warm surfaces) and a dynamic part (AC/ramp losses in the winding, and residual nuclear heating conducted into the cold mass),

$$\dot{Q}_{\text{cryo}} = \underbrace{\dot{Q}_{\text{cond}} + \dot{Q}_{\text{lead}} + \dot{Q}_{\text{rad}}}_{\text{static}} + \underbrace{\dot{Q}_{\text{AC}} + \dot{Q}_{\text{nuc}}}_{\text{dynamic}}.$$

The current-lead term deserves separate treatment because it is optimisable. A metallic lead of length L and cross-section S carrying current I conducts heat down and dissipates Joule heat along its length; the steady conduction equation with a temperature-dependent conductivity $k(T)$ and electrical resistivity $\rho_e(T)$ is

$$\frac{\mathrm{d}}{\mathrm{d}x}\left(k(T)\,S\,\frac{\mathrm{d}T}{\mathrm{d}x}\right) + \frac{I^2\rho_e(T)}{S} = 0.$$

Minimising the cold-end heat leak $\dot{Q}_{\text{lead}} = -kS\,\mathrm{d}T/\mathrm{d}x|_{T_c}$ over the geometry L/S yields the Wiedemann–Franz conduction-optimised limit for a metal lead; replacing the cold section with an HTS lead removes the Joule term below the HTS transition and cuts the per-ampere heat leak by more than an order of magnitude [13], which is the design choice adopted for the breeder cold mass [C1].

Load-balancing as constrained optimisation. As the operating point moves, the several contributions to (11) swing, and the cryoplant must redistribute its refrigeration capacity to hold every cold-mass setpoint. We pose this as: minimise the total wall power subject to holding each temperature node within its band,

$$\min_{\dot{q}_j} \sum_j \frac{\dot{q}_j}{\eta_{\text{plant}}\,\mathrm{COP}_j} \quad \text{s.t.} \quad T_i^{\min} \le T_i(\dot{q}_j) \le T_i^{\max}\ \forall i, \qquad \sum_j \dot{q}_j \ge \dot{Q}_{\text{cryo}},$$

where $\dot{q}_j$ is the cooling delivered at node j and COP_j its local coefficient of performance. Equation (13) is the mathematical statement realised by the cryoplant load-balancer of the control backbone (KFE-CF-SH-120, KFE-CF-BR-026).

VACUUM PUMP-DOWN DYNAMICS

The torus must reach and hold a base pressure low enough that neutral recycling and impurity influx do not spoil the edge. For a chamber of volume V pumped at effective speed S against an outgassing throughput $Q_{\mathrm{out}}(t)$, the zero-dimensional pressure balance is

$$V\,\frac{\mathrm{d}p}{\mathrm{d}t} = -S\,p + Q_{\mathrm{out}}(t), \qquad Q_{\mathrm{out}}(t) = Q_0\,e^{-t/\tau_{\mathrm{out}}} + Q_{\mathrm{floor}}.$$

The homogeneous solution decays with time constant V/S; the particular solution approaches the outgassing-limited base pressure $p_{\mathrm{base}} = Q_{\mathrm{floor}}/S$. The effective speed S is set by the series combination of the pump speed and the duct conductance C, $1/S = 1/S_{\mathrm{pump}} + 1/C$, with C in the molecular-flow regime given by the transmission probability of the duct [29,14]. Equation (14) is the model behind the vacuum-pumping scheduler (KFE-CF-SH-123): it predicts the time to any target pressure and the achievable base, and so schedules the pump-down against the operating calendar.

POWER CONVERSION: TWO ROUTES

Breeder thermal cycle. The breeder converts the $95.2\ MW$ blanket heat through a thermodynamic cycle. Any such cycle is bounded by the Carnot efficiency between the loop outlet T_{hi} and the heat-rejection temperature T_{lo}, $\eta_{\mathrm{Carnot}} = 1 - T_{\mathrm{lo}}/T_{\mathrm{hi}}$; a recuperated closed helium Brayton cycle realises a fixed fraction of this bound, $\eta_{\mathrm{th}} = \zeta\,\eta_{\mathrm{Carnot}}$ with $\zeta \approx 0.6$ for a well-designed recuperated cycle. With $T_{\mathrm{hi}} = 550\ ^{\circ}C$ set by the loop and $T_{\mathrm{lo}} = 35\ ^{\circ}C$, the cycle efficiency lies in the mid-30% range (§6).

Burner direct energy conversion. The separate D–^{3}He tandem-mirror burner converts its charged-particle output *without* a thermal cycle, by electrostatically decelerating the escaping ions on graded collector electrodes [15,16]. The plant-level efficiency is $\eta_{\mathrm{DEC}} = 0.49$, consistent with a module-level direct-conversion efficiency of 0.70 after grid and auxiliary losses [C5]. Direct conversion is available to the burner precisely because its neutron fraction is small ($f_n = 5.44\%$); the breeder, whose power is neutron-dominated, must go through the thermal cycle.

§ 4

Computational methodology: the NVIDIA GPU HPC campaign

The results of this paper were produced on the Kronos NVIDIA GPU HPC campaign (a Lambda fleet of A100/H100/A10 devices) together with an in-house digital-twin node; the split follows the frozen run records in the register.

Codes and problem scale. The volumetric nuclear-heating source $q'''(\quad r)$ that feeds the blanket power split of equation (3) and the loss term $\dot{Q}_{\mathbf{nuc}}$ of equation (11) is computed by Monte-Carlo neutron transport (OpenMC) on a CAD-faithful geometry [10]; GPU acceleration of the transport sweep follows the event-based and GPU-oriented transport methods now established for reactor-scale problems [11], which recast the history loop as data-parallel event kernels to keep the streaming multiprocessors saturated. The post-shutdown decay-heat anchors of equation (7) are grounded in an activation inventory of the FISPACT-II class [9] driven by the same transport solution; at BOP fidelity we use the two-anchor power law and reserve the full inventory for the refinement of §8. The conjugate heat-transfer closure of equations (5)–(6) and the LOFC transient of equation (9) are evaluated in the thermal-fluid twin; the cryogenic load-balancing optimisation of equation (13) and the refrigeration-COP optimiser are trained on the GPU cluster (KFE-CF-SH-122), while the load-balancer, vacuum scheduler and fouling monitor run on the in-house digital-twin node so that the protective loops never contend with the training fleet.

Verification and reproducibility. Solver correctness is established by the method of manufactured solutions and grid-convergence-index study for the discretised transport and thermal operators, and by cross-checking the analytic BOP balances against the twin at the design point. The thermal balance (BR-L1-A9) and the two-magnet ruling (KX-L1-A15) are frozen register entries with independent re-run status; the figure-generation pipeline that produced every data figure here is deposited with the paper and regenerates the numbers from the frozen anchors. No compute-cost quantities are reported; the campaign is described by its codes, GPU acceleration and problem scale only.

§ 5

Numerical formulation and convergence

The one stiff element of the BOP model is the radiative LOFC transient (9): the T^4 sink makes the right-hand side stiff at high temperature, so an explicit integrator would demand impractically small steps. We discretise with the implicit (backward) Euler method, which is A-stable, and solve the resulting nonlinear algebraic equation at each step by Newton iteration. With $T_n \equiv T(t_n)$ and step $\Delta t_n = t_{n+1} - t_n$,

$$T_{n+1} - T_n - \frac{\Delta t_n}{mC}\Big[P_d(t_{n+1}) - \varepsilon\sigma A\big(T_{n+1}^4 - T_{\mathrm{amb}}^4\big)\Big] = 0,$$

and each Newton step uses the analytic derivative

$$\frac{\partial}{\partial T_{n+1}}[\cdots] = 1 + \frac{\Delta t_n}{mC}\,\varepsilon\sigma A\left(4T_{n+1}^3\right),$$

which is strictly positive, so the Newton iteration converges monotonically from the previous-step value. The steady loop balance (4) and the cryogenic optimisation (13) are algebraic and solved to machine tolerance; the vacuum ODE (14) is linear and integrated with the same implicit scheme for unconditional stability across the many-decade pump-down.

We verify the integrator by a self-convergence study against a reference solution computed with 4×10^5 steps. Figure 2 shows the terminal-temperature error falling as $\mathcal{O}(\Delta t)$, confirming first-order accuracy of backward Euler and the correctness of the Jacobian (16). The observed order and the absence of any stability breakdown at large Δt justify the scheme for the safety-relevant transient.

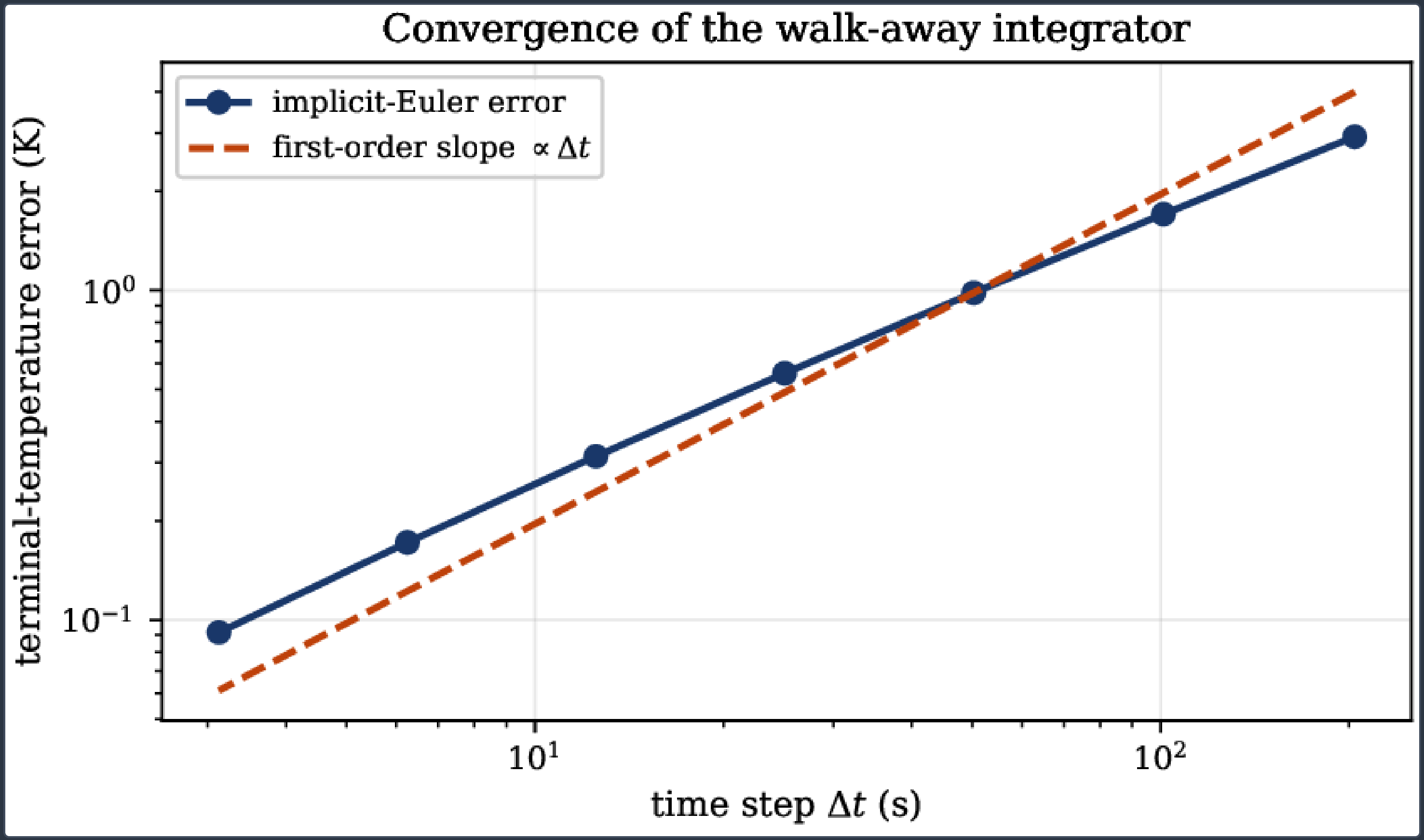

Self-convergence of the implicit-Euler integrator for the loss-of-forced-cooling transient (15): terminal-temperature error versus time step against a 4×10^5-step reference. The error follows the first-order slope $\propto \Delta t$ expected of backward Euler, and no stability breakdown appears at large Δt. Computed from the model of §3.2.

§ 6

Results

POWER BALANCE AND THE COOLANT LOOP

Table 1 collects the breeder BOP design point and figure 3 shows the power split and the coolant-flow relation. The $85.04\,MW$ fusion power divides into $67.79\,MW$ of neutrons and $17.25\,MW$ of charged particles; multiplication by $M_n = 1.15$ in the blanket produces $95.2\,MW$ of thermal power, removed by $91.7\,kg/s$ of helium at $\Delta T = 200\,K$. The Dittus–Boelter film coefficient of equation (5) and the pumping-power scaling of equation (6) are shown in figure 4: at a representative channel Reynolds number the film coefficient is of order $\mathrm{kW\,m^{-2}K^{-1}}$, and a $\sim 0.3\,MPa$ loop pressure drop keeps the pumping fraction to a few percent of the thermal power.

QUANTITY	VALUE
fusion power P_{fus}	$85.04\,MW$
neutron power P_n	$67.79\,MW$
charged-particle power P_{chg}	$17.25\,MW$
energy multiplication M_n	1.15
blanket thermal power P_{th}	$95.2\,MW$
He coolant mass flow $\dot{m}$ ($\Delta T = 200\,K$)	$91.7\,kg/s$
inlet volumetric flow $\dot{V}_{\text{in}}$ (8 MPa, 350 °C)	$\approx 14.8\,m^3/s$
decay heat at 1 s / 1	$0.95\,MW$ / $95\,kW$

Breeder balance-of-plant design point. Source: register serial BR-L1-A9 [31].

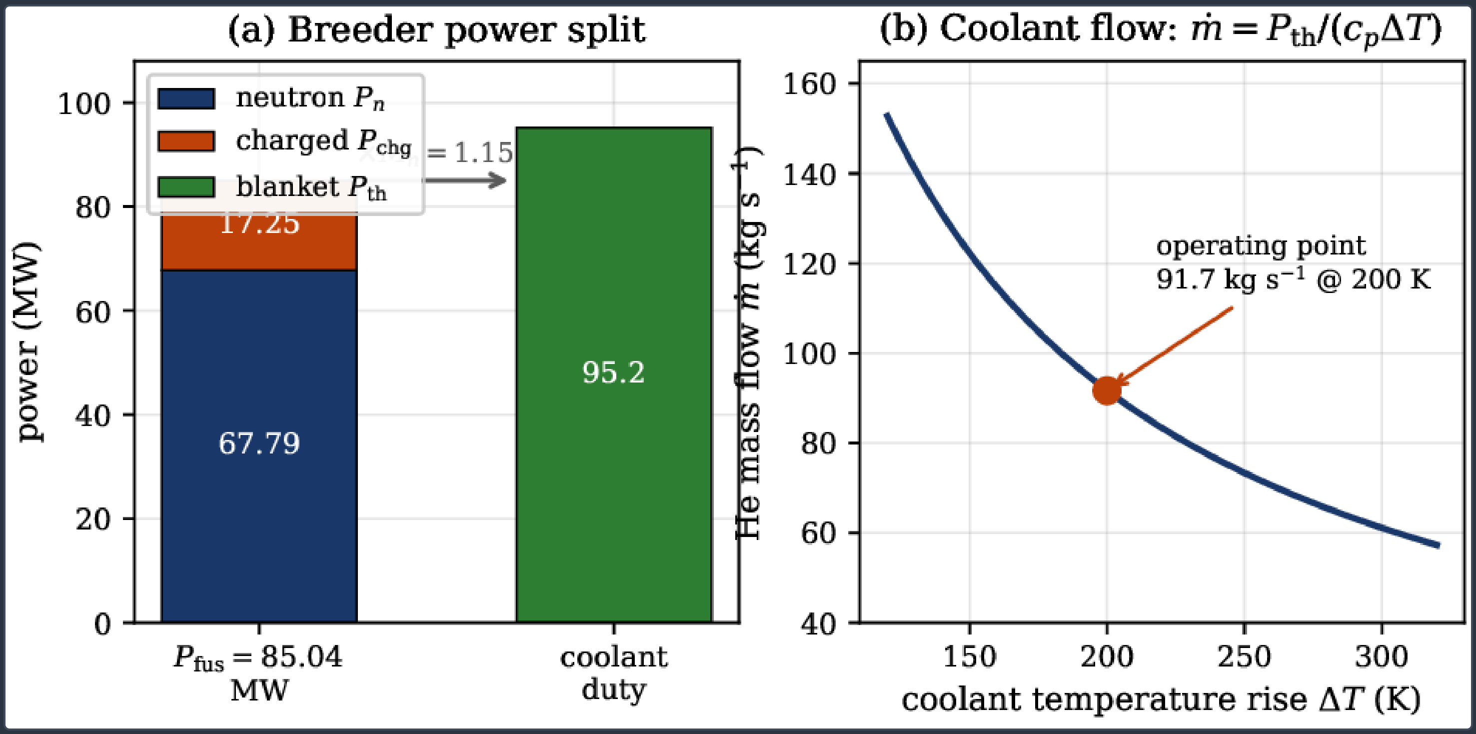

Breeder power balance and coolant duty. (a) $P_{\text{fus}} = 85.04\,MW$ splits into neutron and charged-particle power; blanket multiplication ($M_n = 1.15$) yields $P_{\text{th}} = 95.2\,MW$. (b) The coolant mass flow $\dot{m} = P_{\text{th}}/(c_p \Delta T)$; the operating point ($91.7\,kg/s$ at $\Delta T = 200\,K$) is marked. Data from BR-L1-A9.

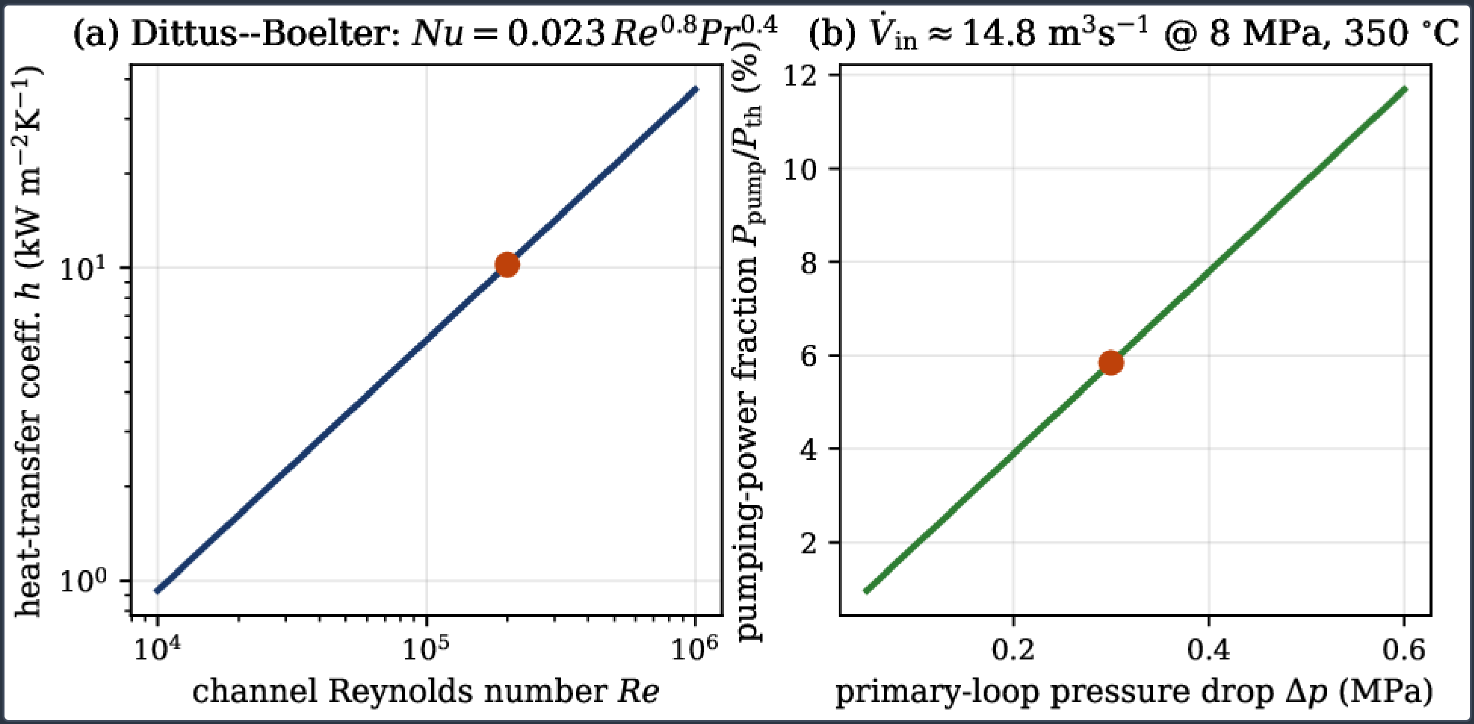

Primary helium loop. (a) Dittus–Boelter film coefficient h versus channel Reynolds number, equation (5). (b) Pumping-power fraction versus loop pressure drop from the scaling of equation (6), with the inlet volumetric flow $\dot{V}_{\mathrm{in}} \approx 14.8\, m^3/s$; markers show a representative operating point. Curves are design-basis physics, not measurements.

PASSIVE DECAY-HEAT REJECTION

The safety result is shown in figures 5 and 6. The decay heat follows $P_d(t) \propto t^{-0.203}$ through the two frozen anchors; the radiative-equilibrium wall temperature of equation (8) stays below the $\approx 710\ ^{\circ}C$ sub-damage ceiling for all times, reaching $\approx 711\ ^{\circ}C$ at the one-second peak and $\approx 290\ ^{\circ}C$ at one day. The LOFC transient of equation (9), integrated with the implicit scheme of §5, lies far below the zero-thermal-mass quasi-static bound (figure 6): finite thermal inertia smears the source, so the realised peak temperature is well inside the safe envelope. The machine therefore survives a complete loss of forced cooling by radiation and conduction alone. The estimate is conservative twice over: it uses only the compact plasma-facing area (the real vessel and cryostat area is larger) and neglects conduction paths that add further margin.

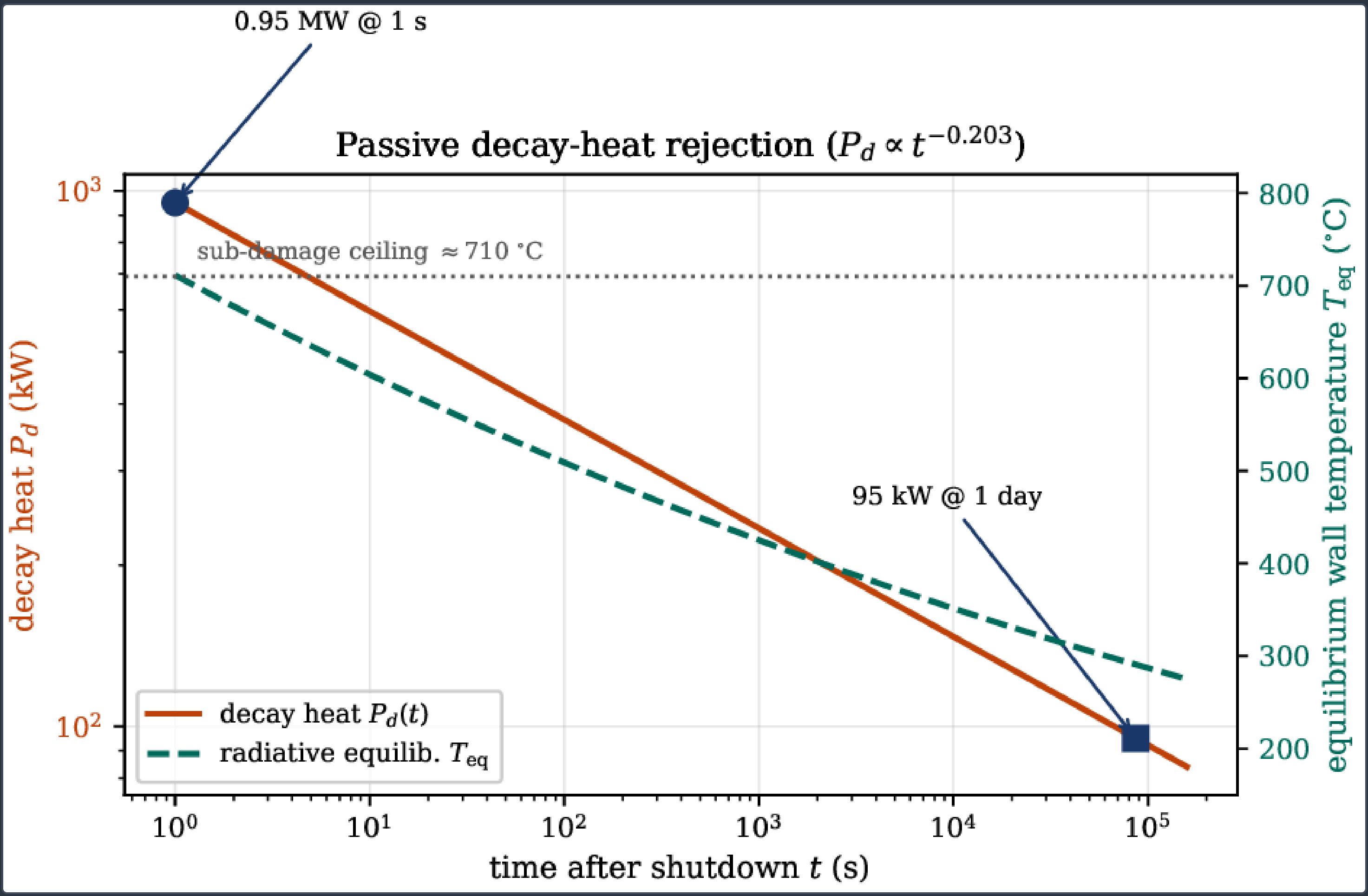

Post-shutdown decay heat $P_d(t)$ (left axis) through the frozen anchors $0.95\ MW$ at 1 s and $95\ kW$ at one day, with power-law exponent $\alpha = 0.203$, and the corresponding radiative-equilibrium wall temperature T_{eq} (right axis) from equation (8). T_{eq} never crosses the $\approx 710\ ^{\circ}C$ sub-damage ceiling. Data from BR-L1-A9.

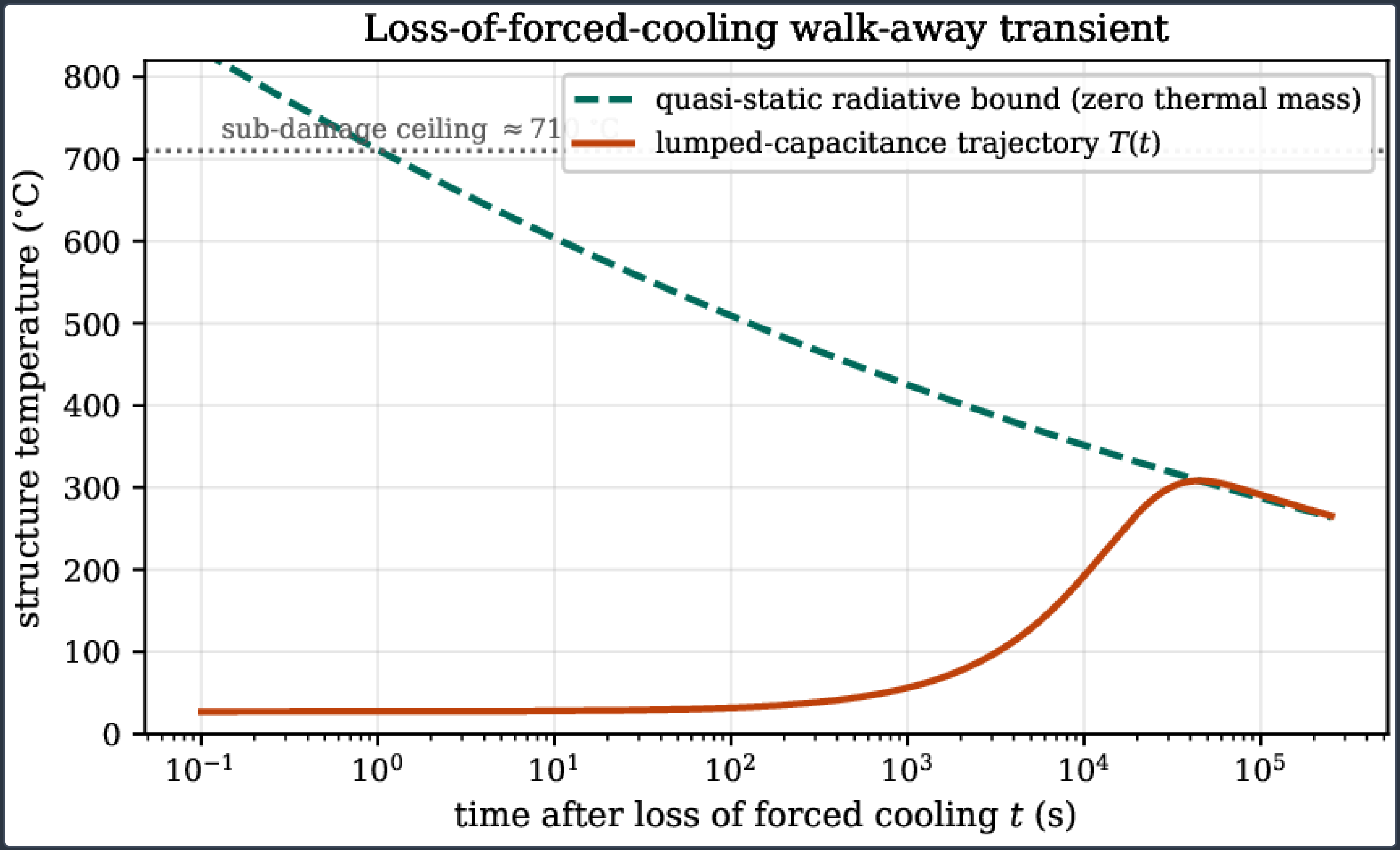

Loss-of-forced-cooling walk-away transient. The lumped-capacitance trajectory $T(t)$ from equation (9) (solved by implicit Euler, §5) lies well below the quasi-static zero-thermal-mass radiative bound, and both remain under the $\approx 710\,^{\circ}C$ ceiling. Computed from the model of §3.2 with a representative structure heat capacity.

THE CRYOGENIC ENVELOPE AND THE TWO DISTINCT MAGNETS

The cryogenic load is dominated by the cold mass, and the cold mass is set by *two distinct* magnets, which the design keeps rigorously separate (KX-L1-A15). The breeder centrepost governs at a peak field of $16.84\,T$ — its own device — with a current-sharing temperature margin of $49.5\,K$ at a load fraction $I_{\mathrm{op}}/I_c = 0.27$; the burner plug coil of the separate burner product is a distinct, higher-field magnet at $26.49\,T$ with margin $37.1\,K$ at load fraction 0.43 (table 2, figure 7). Conflating the centrepost field with the plug field would misstate the cryogenic load and the magnet-integrity case; keeping them separate is load-bearing. The refrigeration penalty of equation (10) is shown in figure 8(a): at $4.5\,K$ each watt in the cold mass costs ≈ 219 W of input at 30% Carnot, so the load budget of figure 8(b) — support conduction, current leads, AC/ramp losses, radiation and residual nuclear heating — is the quantity the load-balancer of equation (13) minimises.

MAGNET	MACHINE	GOVERNING FIELD	MARGIN / LOAD FRACTION
centrepost	breeder	$16.84\,T$	$49.5\,K$ / 0.27
plug coil	burner	$26.49\,T$	$37.1\,K$ / 0.43

Two distinct magnets set the cryogenic envelope. Source: register serial KX-L1-A15 [31].

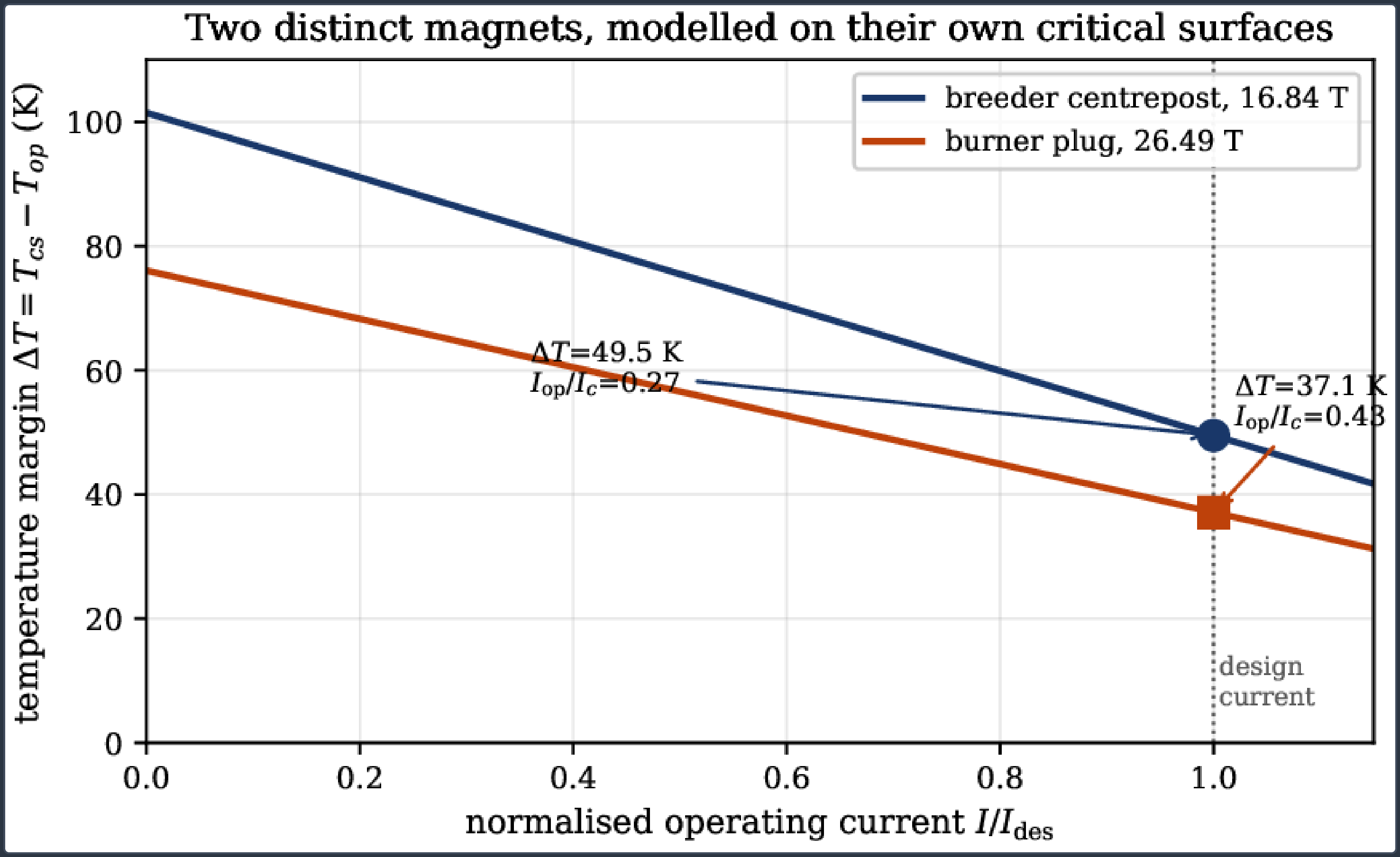

Temperature-margin load lines of the two distinct magnets, each modelled on its own critical surface (KX-L1-A15). Markers at the design current: breeder centrepost $\Delta T = 49.5\,K$ at $16.84\,T$ (load fraction 0.27); burner plug $\Delta T = 37.1\,K$ at $26.49\,T$ (load fraction 0.43). The protective observable is the drift of ΔT toward the current-sharing line.

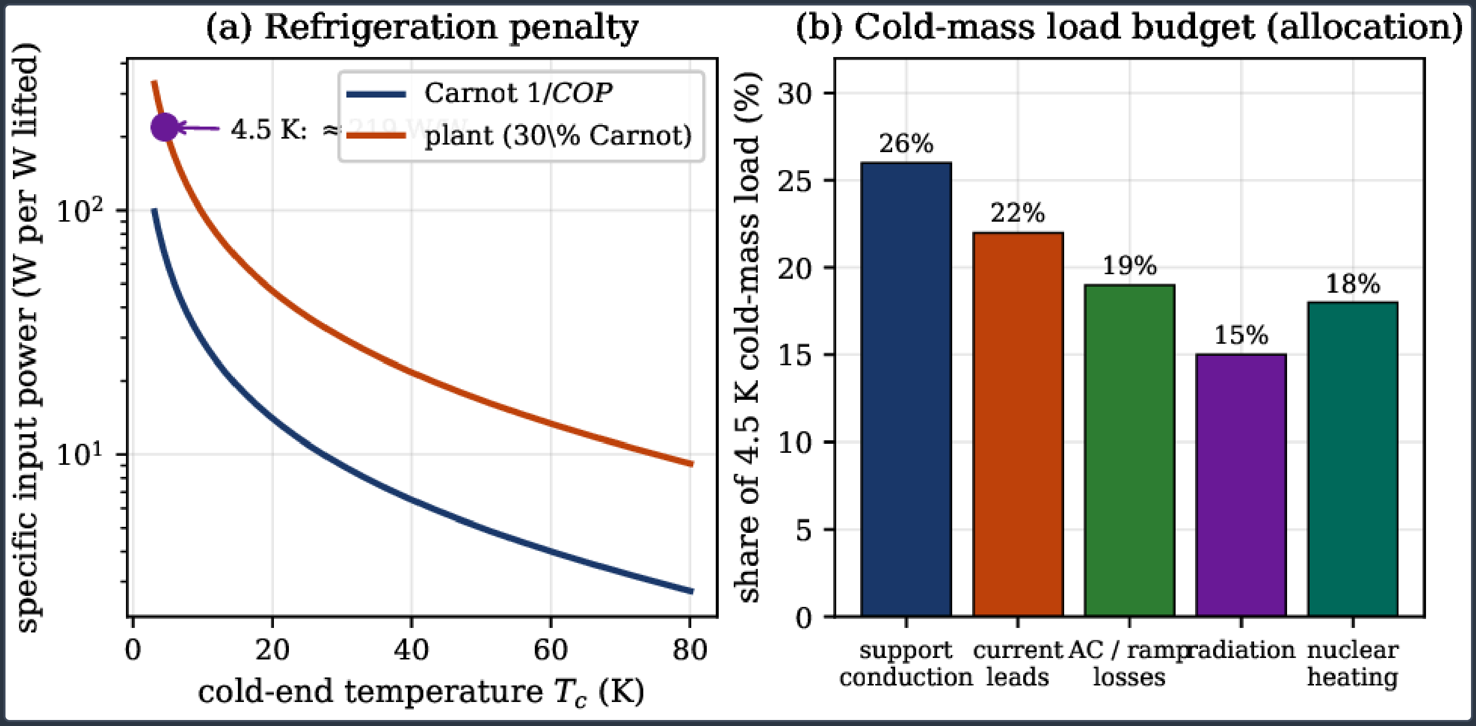

Cryogenic envelope. (a) Refrigeration specific input power (W per W lifted) versus cold-end temperature — Carnot and 30%-Carnot plant — from equation (10); the $4.5\,K$ operating point ($\approx 219\ \mathrm{W\,W^{-1}}$) is marked. (b) Representative allocation of the $4.5\,K$ cold-mass load across its static and dynamic contributions, equation (11); the load-balancer minimises the wall power that serves this budget.

VACUUM SCHEDULING

Figure 9 shows the pump-down solution of equation (14): the pressure falls through the exhaust time constant V/S toward an outgassing-limited base of $\sim 1e-7\,Pa$, passing $1e-3\,Pa$ within a few seconds for the representative chamber and pumping speed. The scheduler predicts the time to any target pressure and so places the pump-down against the operating calendar; the base pressure is set by the outgassing floor Q_{floor}/S, which motivates bake-out and low-outgassing surface preparation rather than brute pumping speed.

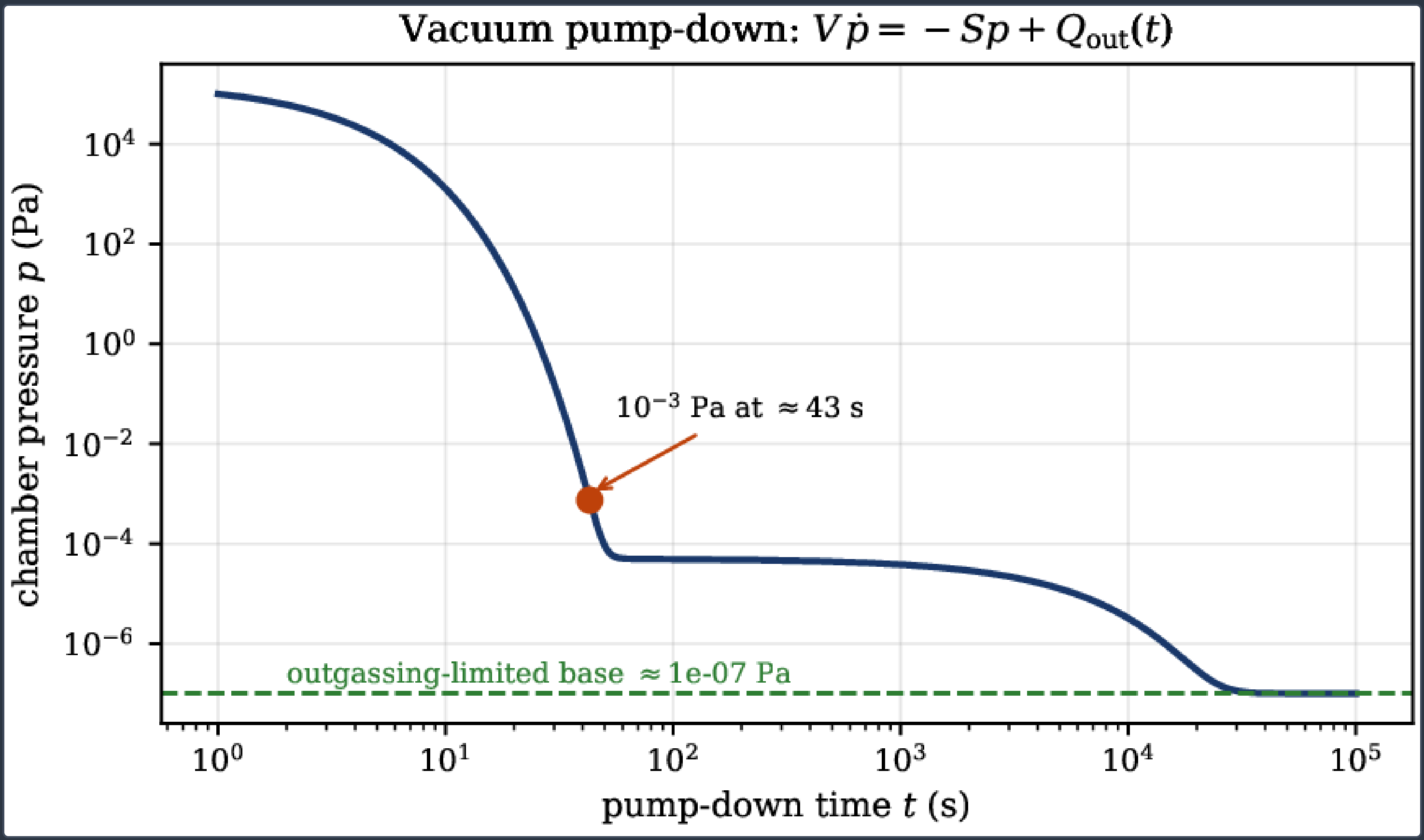

Vacuum pump-down from the model $V\dot{p} = -Sp + Q_{\text{out}}(t)$, equation (14), integrated with the implicit scheme of §5. The pressure reaches the outgassing-limited base $p_{\text{base}} = Q_{\text{floor}}/S$; the time to $1e-3\,Pa$ is marked. Design-basis physics for a representative chamber and pumping speed.

POWER CONVERSION ROUTES

Figure 10 contrasts the two conversion routes. The breeder thermal cycle (figure 10a) is bounded by Carnot and realises $\zeta \approx 0.6$ of it for a recuperated helium Brayton cycle; at the loop outlet of $550\ ^{\circ}C$ the cycle efficiency lies in the mid-30% range. The burner direct energy converter (figure 10b) reaches a plant efficiency $\eta_{\rm DEC} = 0.49$, consistent with a module-level 0.70 after grid and auxiliary losses — available to the burner because its neutron fraction is small, and unavailable to the neutron-dominated breeder.

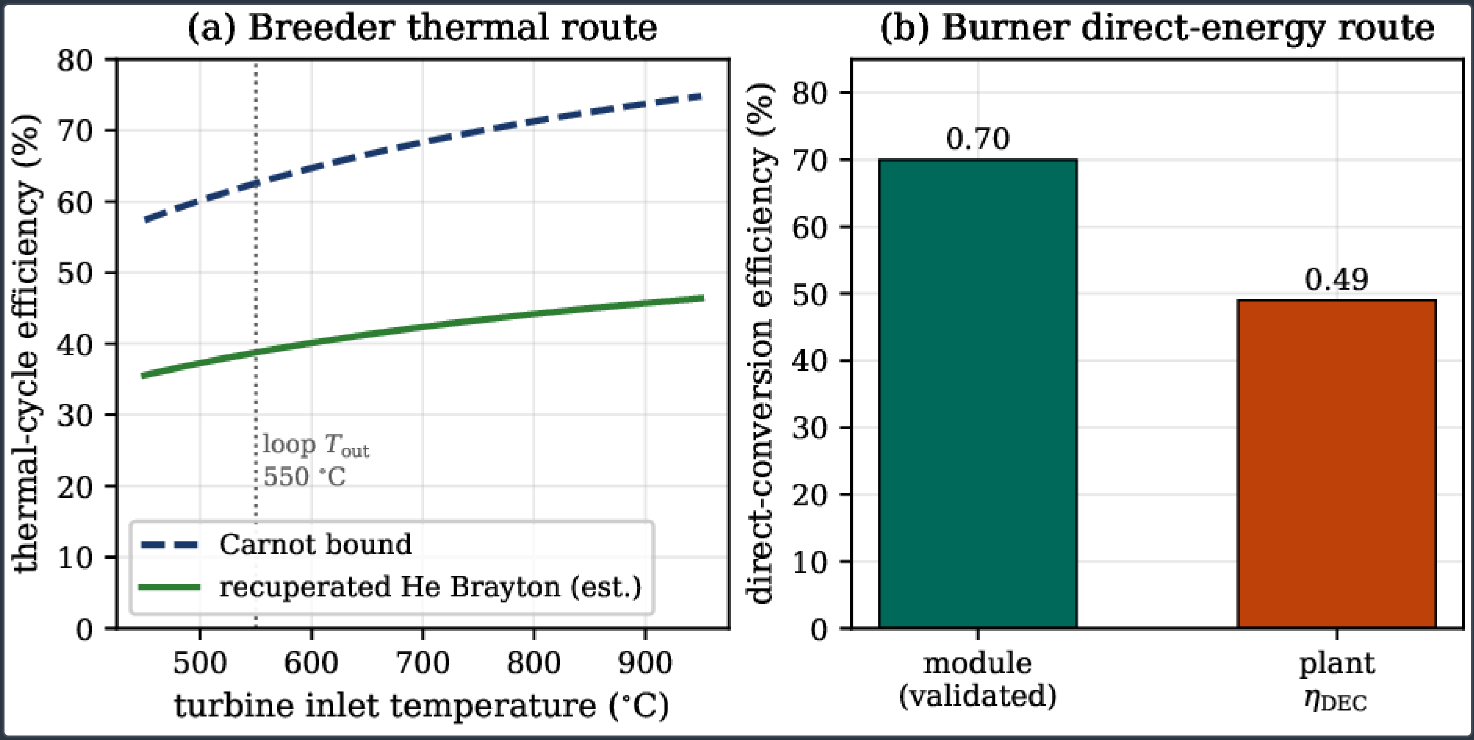

Two power-conversion routes. (a) Breeder thermal cycle: Carnot bound and recuperated He Brayton estimate ($\zeta \approx 0.6$) versus turbine inlet temperature, with the $550\ ^{\circ}C$ loop outlet marked. (b) Burner direct energy conversion: validated module efficiency 0.70 and plant efficiency $\eta_{\rm DEC} = 0.49$. Data from the design point and the direct-energy-conversion companion study [C5].

THE CRYO-VACUUM CONTROL BACKBONE

On the demonstrated thermal and magnet envelope we build the cryo-vacuum control backbone (table 3, figure 12): a cryoplant load-balancer that holds cryogenic margin under load swings (equation (13); KFE-CF-SH-120), a refrigeration-COP optimiser that improves the coefficient of performance at fixed load (KFE-CF-SH-122), a vacuum-pumping scheduler that reaches base pressure on schedule (equation (14); KFE-CF-SH-123), and a heat-exchanger fouling monitor that flags a fouling trend before it reaches its limit (figure 11; KFE-CF-SH-125). Each is gated by a single common criterion — cryogenic setpoints held while the BOP heat-and-power balance closes within tolerance — and each is built to the demonstrated envelope above. The load-balancer, scheduler and fouling monitor run on the in-house digital-twin node; the efficiency optimiser runs on the NVIDIA GPU HPC campaign.

The fouling monitor is grounded in the effectiveness–NTU model. Fouling adds a resistance R_f in series with the clean overall coefficient, $1/U = 1/U_0 + R_f$, and the exchanger effectiveness for the relevant limit is $\varepsilon = 1 - \exp(-\mathrm{NTU})$ with $\mathrm{NTU} = UA_{\rm hx}/(\dot{m}c_p)$; figure 11 shows both degrading with R_f and the alarm threshold placed before the effectiveness knee.

COMPONENT	FUNCTION	GOVERNING MODEL	ACCEPTANCE TEST
cryoplant load-balancer	hold cryo margin	eq. (13)	margin held under load swings
refrigeration-COP optimiser	improve efficiency	eq. (10)	COP improved at fixed load
vacuum-pumping scheduler	reach base pressure	eq. (14)	base pressure on schedule
heat-exchanger fouling monitor	protect the loop	ε–NTU	fouling flagged before limit

The cryo-vacuum control backbone: each component built to the demonstrated thermal/magnet envelope and gated by a common acceptance criterion. Source: register serials KFE-CF-SH-120/122/123/125 [31].

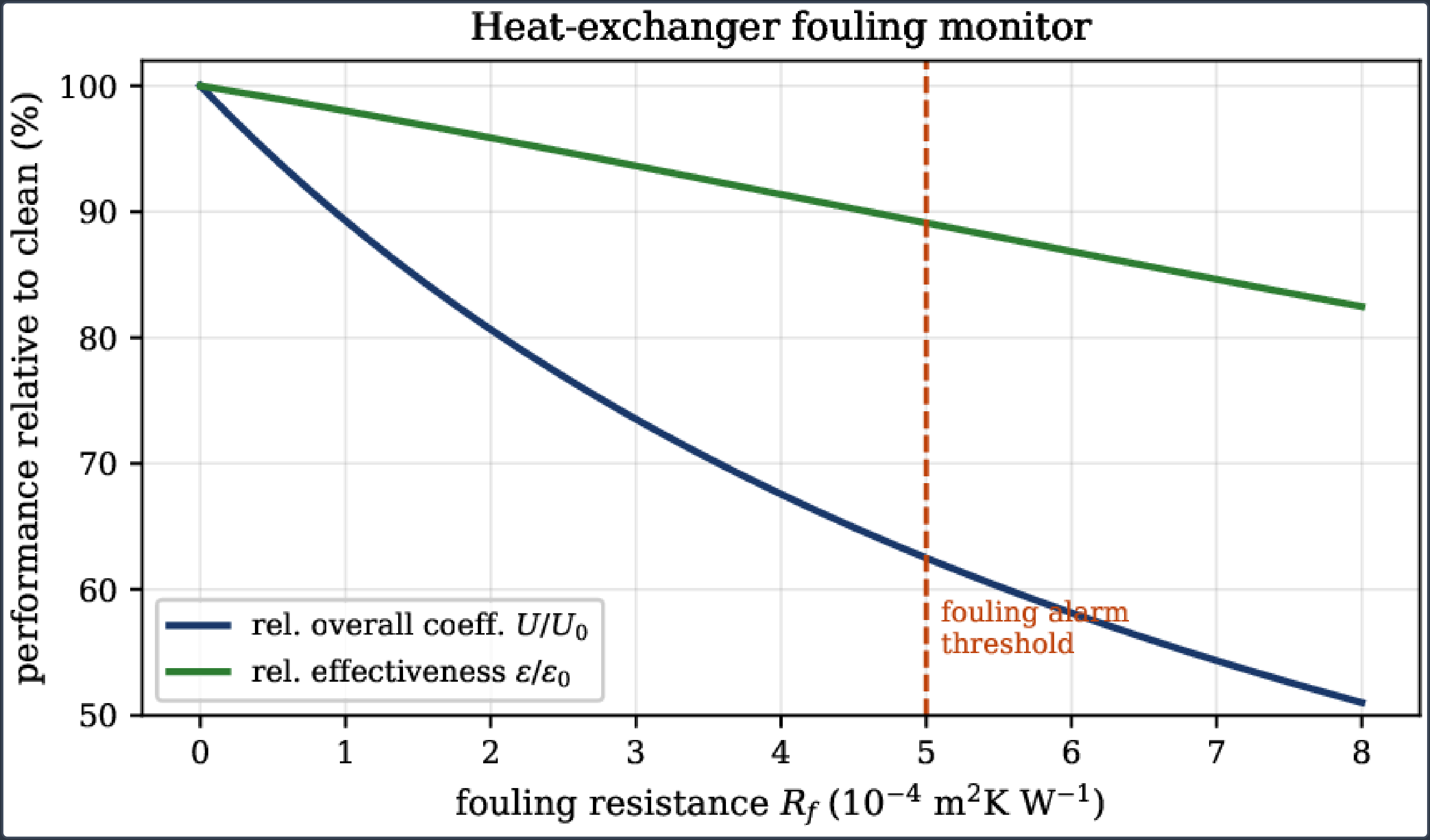

Heat-exchanger fouling monitor. Relative overall coefficient $U/U_0 = [1 + U_0 R_f]^{-1}$ and relative effectiveness $\varepsilon/\varepsilon_0$ versus fouling resistance R_f, with the alarm threshold set before the effectiveness knee. Design-basis ε–NTU model (KFE-CF-SH-125).

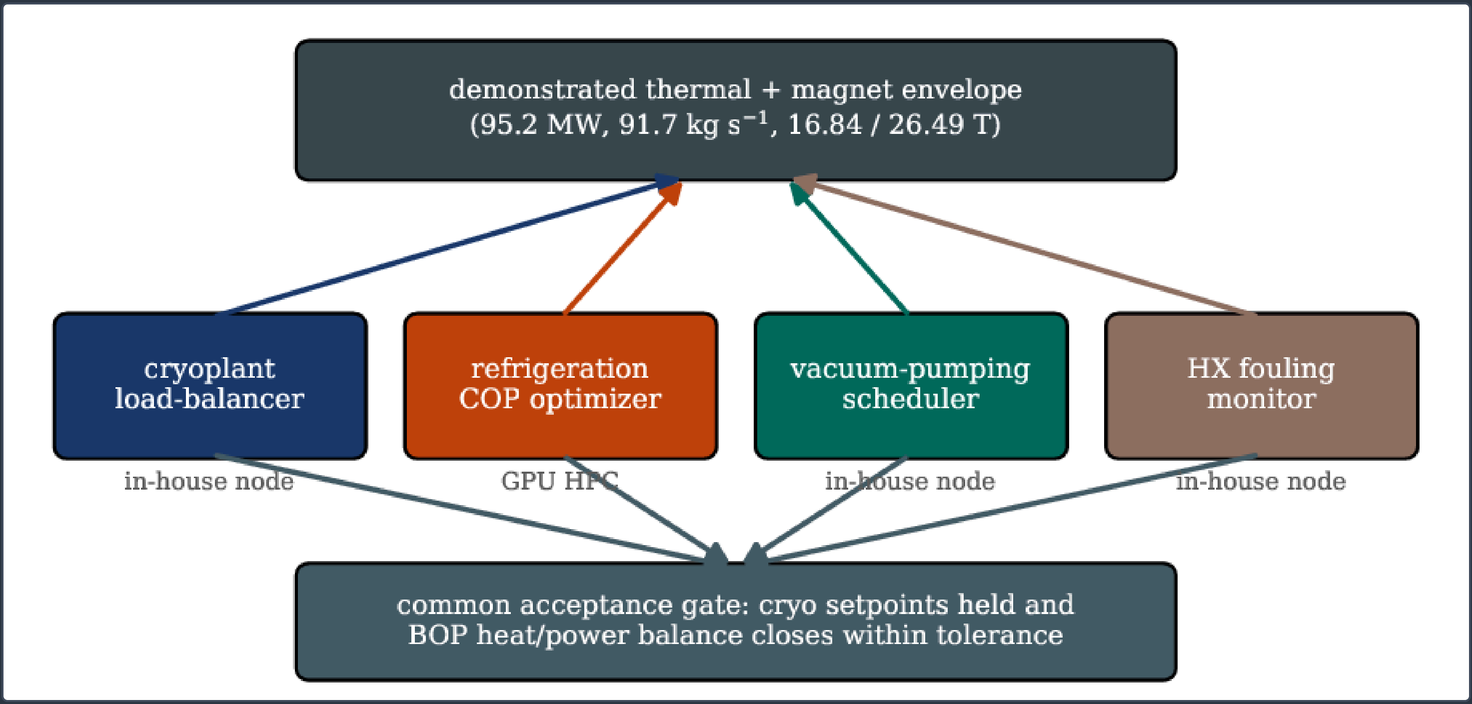

(Schematic.) The cryo-vacuum control backbone. Each of the four components is built to the demonstrated thermal and magnet envelope (top) and gated by the common acceptance criterion (bottom); host assignment (in-house node vs GPU HPC) is annotated. The envelope and criterion are the real, frozen bars; the layout is schematic.

§ 7

Discussion

BENCHMARKS AGAINST PUBLISHED PLANT DESIGNS

The BOP picture is coherent and quantitatively consistent with the published fusion-plant literature, while being sized to a much more compact machine. The high-pressure helium primary loop — $8\,MPa$, inlet/outlet §Irange350550 — is the same class of coolant conditions adopted by the EU DEMO HCPB blanket [6,4], and the blanket energy-multiplication factor $M_n = 1.15$ sits within the range reported for Li/Be-bearing blankets. The coolant duty follows directly from the first law (equation (4)) and carries no modelling freedom once P_{th} and ΔT are fixed. The passive decay-heat result is where the compact ST differs most favourably from a large plant: the ratio of decay heat to radiating area is what matters, and because the Kronos blanket power ($\approx 95\,MW$) is an order of magnitude below a DEMO-class plant while the plasma-facing area is not correspondingly smaller, the equilibrium temperatures of equation (8) fall below the damage threshold. This is the same activation-dominated decay physics used in DEMO safety analyses [8], applied to a machine whose power density makes passive rejection reachable.

On the cryogenic side, the $\approx 219\ \mathrm{W\,W^{-1}}$ plant specific power at $4.5\,K$ is the standard figure for large helium refrigeration [12], and the decision to carry the current-lead heat leak on HTS leads [13] is the same lever the accelerator and tokamak communities use to hold the static load down. The torus vacuum model reproduces the outgassing-limited base-pressure behaviour that rarefied-gas analyses of ITER-class cryopumps predict [14]. The direct-energy-conversion route for the burner is grounded in the experimental direct-converter line [15] and the mirror programme [16], with the 0.49 plant efficiency a conservative read of the module-level 0.70.

WHY THE TWO-MAGNET SEPARATION MATTERS FOR THE BOP

A recurring error in compact-ST discussions is to quote a single peak field for “the magnet”. The Kronos design has two distinct high-field magnets belonging to two distinct products: the breeder centrepost at $16.84\,T$ and the burner plug coil at $26.49\,T$. For the BOP this is not a naming nicety — it sets the cold-mass load, the current-lead rating, and the quench-energy budget, all of which differ between the two devices. Treating them as one would either overstate the breeder cold-mass load (if the plug field were used) or understate the burner's (if the centrepost field were used). The load-balancer of equation (13) is therefore configured per magnet, on each device's own critical surface (figure 7) [C1,C6].

THE CONTROL BACKBONE HAS CONCRETE TARGETS

Because the envelope is demonstrated and the acceptance criterion is single and testable, each backbone component maps to a governing equation (table 3) and to a frozen register serial; the four-twin control architecture that hosts them [C4] admits each to authority only after it holds cryogenic setpoints while the plant balance closes — the same maturity-gated discipline used across the Kronos control stack.

§ 8

Limitations

One honest gate bounds the decay-heat claim. The $M_n = \mathbf{1.15}$ blanket energy multiplication and the two-anchor power-law decay curve of equation (7) are BOP-level surrogates for a full, isotope-resolved activation-inventory (FISPACT-II-class [9]) calculation on the as-built material inventory. A dedicated activation-inventory study is the honest next step; it is expected to refine the shape of the decay-heat curve without overturning the passive-rejection conclusion, which already carries conservative-area margin (the compact plasma-facing area only) and a finite-thermal-mass transient that sits well below the quasi-static bound.

§ 9

Conclusion

We have formalised the balance of plant of the Kronos Hyperion breeder as a coupled thermal–fluid–cryogenic–vacuum system and reduced it to governing equations, a numerical formulation, and a demonstrated design envelope. At the ratified design point the blanket dissipates $95.2\,MW$, removed by $91.7\,kg/s$ of helium at $\Delta T = 200\,K$. The decisive result is passive safety: decay heat falling as $t^{-0.203}$ from $0.95\,MW$ at 1 s to $95\,kW$ at one day is rejected by radiation and conduction at sub-damage wall temperatures ($\approx 711\,^{\circ}C$ and $\approx 290\,^{\circ}C$), and the finite-thermal-mass transient lies far below that conservative bound, so the machine survives a complete loss of forced cooling with no forced post-shutdown cooling required. The cryogenic envelope is set by two distinct magnets — the breeder centrepost at $16.84\,T$ and the burner plug at $26.49\,T$ — and the $4.5\,K$ refrigeration penalty ($\approx 219\ \mathrm{W\,W^{-1}}$) makes minimising the cold-mass load the governing cryogenic objective; vacuum scheduling reaches an outgassing-limited base of $\sim 1e-7\,Pa$; and power conversion runs by a breeder thermal cycle and a burner direct converter at plant efficiency 0.49. On this demonstrated envelope we define the cryo-vacuum control backbone — load-balancer, COP optimiser, vacuum scheduler and fouling monitor — each mapped to a governing equation and gated by holding cryogenic setpoints while the plant balance closes within tolerance.

Acknowledgments tocsectionAcknowledgments Part of the Kronos Fusion Energy 2026 design series. The thermal, magnet and cryo-vacuum analyses used the NVIDIA GPU HPC campaign and the in-house digital-twin node. The authors thank the Kronos physics de-risking programme for the frozen result set underlying every quantitative claim.

Reproducibility. The thermal-hydraulic and decay-heat design point (BR-L1-A9) and the two-magnet ruling (KX-L1-A15) are frozen entries in the Kronos Physics De-Risking Register [31] (doi:10.5281/zenodo.22133057) and are regenerable from the archived toolkit configuration and the figure-generation pipeline deposited with this paper. This paper is archived at its DOI doi:10.5281/zenodo.22645901 and its official page https://www.kronosfusionenergy.com/publications/balance-of-plant-for-a-compact-spherical-tokamak-breede.html.

Data availability tocsectionData availability The power balance, decay-heat curve, magnet load lines, cryogenic and vacuum models used for the figures are archived with the deposit at doi:10.5281/zenodo.22645901, which references the Kronos 2026 series — including the cold-mass cryogenics study [C1], the blanket/divertor thermal-hydraulics and walk-away case [C2], and the four coupled digital twins [C4]. All quantitative values trace to the register [31] (doi:10.5281/zenodo.22133057) by the serial identifiers cited inline. Any economic analysis is reported separately and is not part of the public deposit.

Competing interests tocsectionCompeting interests Provisional patent applications relating to aspects of this work have been filed.

tocsectionReferences

Portfolio, People & Record

The intellectual-property estate, the people who built it, the limitations that gate it, and the sources it rests on.

1	4	40	27
GRANTED PATENT	2026 PROVISIONALS	TEAM MEMBERS	2022 PROVISIONALS

INTELLECTUAL PROPERTY

The patent portfolio

The estate spans a granted high-field magnet patent, pending utility and 2026 provisional filings that map to the two products, a digital-twin control provisional, a registered trademark application, and the original 2022 provisional family. Every patentable disclosure in the five-paper arXiv drop was protected **before** publication: the breeder and burner provisionals were filed 1–2 August, and a publication-gap omnibus filing the evening before the drop swept up the DEC, plasma-control, and REBCO-winding matter of the three otherwise-unprotected papers. Patent numbers and application serials are matters of public record; claim scope is summarised, not reproduced.

GRANTED & PENDING UTILITY

US 12,009,112	High-field tilted graded-REBCO magnet architecture (KRONO-002A) · *app. 17/878,550*	GRANTED
US 17/878,507	Core device / method (KRONO-001A) · *utility*	PENDING

2026 PROVISIONAL FILINGS — MAPPED TO THE PRODUCTS

64/124,209	Hyperion — spherical-tokamak tritium / helium-3 foundry · *breeder · filed Aug 2026*	FILED
64/124,220	Aegis / MetroVolt — synchrotron-cutoff, fuel-selection & plug-winding · *generator · filed Aug 2026*	FILED
64/115,167	KRONOS-CTRL digital-twin plant control · *provisional · filed Jul 2026*	FILED
64/005,440	Integrated spherical-tokamak fusion architecture · *early integrated-architecture filing · filed Mar 2026*	FILED
64/105,530	Negative-triangularity spherical-tokamak architecture · *foundational ST filing · filed Jul 2026*	FILED
64/128,097	Publication-gap omnibus — quasineutral two-species expander DEC · provenance-gated / latency-split plasma control · as-built high-field winding & conductor architecture · *filed 7 Aug 2026, the evening before the arXiv drop*	FILED

TRADEMARK & ORIGIN

FTK-98801894	Kronos Fusion Energy — trademark application	FILED
KR-2022-*	Original provisional family (KR-2022-00001 … 00027) · *27 filings, 2022*	PRIORITY

The narrow, defensible magnet novelty — the specific conductor and the digital-twin winding optimisation, not high-field REBCO as a category — is the commercial core that can earn ahead of any $Q > 1$ milestone, with markets in fusion magnet supply, MRI/NMR, accelerators, and proton therapy. The claim is scoped honestly: the high field is a *system field* result, not a stand-alone-coil record; the small-bore plug coil is structurally infeasible as a bare winding but resolved by a stress-managed structural shield (feasible-pending-FEA); and the winding-tape experiment returned a *null result*. The value is the method, not a field record.

THE TEAM

Founding partners, board, advisors & auditors

Kronos is built by a bench of advanced-fuel-fusion, high-field-magnet, direct-conversion, and materials specialists, with a board and operations team drawn from defense, national laboratories, and industry. Dates are shown as ranges; where a tenure has ended or is term-ending, the range says so.

FOUNDING PARTNERS — SCIENCE

Dr. Gerald Kulcinski
Co-Founder · Helium-3 & Advanced-Fuel Fusion
UW–Madison · 2023–Present

Dr. Carl Weggel
Chief Scientist / S.M.A.R.T. Design
MIT Alcator Program · 2022–Present

Dr. Robert J. Weggel
Magnetic Field Design
MIT Magnet Lab · 2022–Present

BOARD

Priyanca Ford
Founder & CEO · Executive Board
2022–Present

Bandel Carano
Finance / Strategy
Oak Investment Partners / Stanford · 2025–2026

Patrick Schweiger
Fusion Device Engineering
Oklo / CFS / TerraPower · 2025–Present

SCIENTIFIC ADVISORS

Dr. Steven O. Dean
Fusion Policy & History
DOE / Fusion Power Associates · 2025–Present

Dr. Patrick H. Diamond
Plasma Turbulence & Transport
UC San Diego · 2025–Present

Dr. Jack J. Dongarra
HPC & Numerical Algorithms
Turing Award · 2025–Present

Dr. Nasr M. Ghoniem
Chief Material Scientist
UCLA · 2025–Present

Dr. Siegfried Glenzer
Plasma Physics & Laser Fusion
Stanford / SLAC · 2022–Present

Dr. David A. Hammer
Pulsed-Power Fusion
Cornell · 2025–Present

Dr. Donald A. Spong
Plasma Theory & Confinement
ORNL · 2025–Present

Dr. Curtis Smith
Risk Assessment & Nuclear PRA
MIT / Idaho National Lab · 2025–Present

RADM (Ret.) David Goggins
Naval Engineering & Power-Plant Design
U.S. Navy · 2023–2026

Dr. Konstantin Batygin
Mathematician
Caltech · 2022–2025

Dr. Ruben Fair
Magnet Design / ITER Liaison
PPPL / Jefferson Lab · 2022–2025

Dr. Paul S. Weiss
Materials & Nanotechnology
UCLA · 2022–2025

SCIENTIFIC AUDITORS

Dr. Wilfred A. Cooper
Plasma Equilibrium Theory
EPFL / Swiss Plasma Center · 2025–Present

Dr. Ahmed Hassanein
Plasma–Material Interactions
Purdue / Argonne · 2025–Present

Dr. Patrick E. Hopkins
Extreme Thermal Materials
U. of Virginia · 2025–Present

Dr. Peter Hosemann
Materials Joining & Structural Integrity
UC Berkeley · 2025–Present

Dr. Travis W. Knight
Advanced Nuclear Fuels & Systems
U. of South Carolina · 2025–Present

Dr. Philippe Lebrun
Cryogenics & Magnet Cooling
CERN · 2025–Present

Dr. Nitendra Singh
Nuclear Safety & Fuel Cycle
ITER · 2025–Present

Dr. Guido Van Oost
Magnetic Confinement & Fusion Systems
Ghent University · 2025–Present

Dr. Gary S. Was
Radiation Materials & Structural Integrity
U. of Michigan · 2025–Present

Dr. Ray Sedwick
Direct Energy Conversion
U. of Maryland · 2025

OPERATIONS

Michael Laughlin
Chief Operating Officer
2022–Present

Martin Owens
Chief Strategy Officer
LANL / GE Hitachi · 2022–Present

MG (Ret.) Paul Pardew
Chief Contracting Officer
Army Contracting Command · 2022–Present

David Beck
Fusion Commercialization
U.S. Space Force · 2024–Present

Sushma Bhatia
Environmental & Legislative
Google · 2022–Present

Michael De Frenza
Technology Licensing
2023–Present

MG (Ret.) Robin L. Fontes
Cybersecurity & Defense
Army Cyber Command · 2022–Present

Vijay Gehani
Supply Chain & Components
INOX India · 2024–Present

Jon Michel Greenwood
IT & AI Infrastructure
Live Nation · 2023–Present

Brian C. O'Neill
National Security
CIA / ODNI · 2022–Present

Gen. (Ret.) Gustave F. Perna
DoD Liaison
Operation Warp Speed · 2022–2023

Andrea Romero
Marketing Lead
2022–Present

Legal counsel is retained; those roles are held on the internal roster and are not listed here.

SOURCES

References

1 J E Menard *et al*, Fusion nuclear science facilities and pilot plants based on the spherical tokamak, *Nucl. Fusion* **56** 106023 (2016). doi:10.1088/0029-5515/56/10/106023

2 B N Sorbom *et al*, ARC: a compact, high-field, fusion nuclear science facility and demonstration power plant with demountable magnets, *Fusion Eng. Des.* **100** 378 (2015). doi:10.1016/j.fusengdes.2015.07.008

3 A J Creely *et al*, Overview of the SPARC tokamak, *J. Plasma Phys.* **86** 865860502 (2020). doi:10.1017/S0022377820001257

4 G Federici *et al*, Overview of EU DEMO design and R&D activities, *Fusion Eng. Des.* **89** 882 (2014). doi:10.1016/j.fusengdes.2014.01.070

5 D Maisonnier *et al*, DEMO and fusion power plant conceptual studies in Europe, *Fusion Eng. Des.* **81** 1123 (2006). doi:10.1016/j.fusengdes.2005.08.055

6 F A Hern\'andez, P Pereslavtsev *et al*, An enhanced, near-term HCPB design as driver blanket for the EU DEMO, *Fusion Eng. Des.* **146** 1186 (2019). doi:10.1016/j.fusengdes.2019.02.037

7 M Abdou *et al*, Physics and technology considerations for the deuterium–tritium fuel cycle and conditions for tritium fuel self sufficiency, *Nucl. Fusion* **61** 013001 (2021). doi:10.1088/1741-4326/abbf35

8 M R Gilbert, T Eade, C Bachmann, U Fischer and N P Taylor, Activation, decay heat, and waste classification studies of the European DEMO concept, *Nucl. Fusion* **57** 044002 (2017). doi:10.1088/1741-4326/aa5bd7

9 J-Ch Sublet, J W Eastwood, J G Morgan, M R Gilbert, M Fleming and W Arter, FISPACT-II: an advanced simulation system for activation, transmutation and material modelling, *Nucl. Data Sheets* **139** 77 (2017). doi:10.1016/j.nds.2017.01.002

10 P K Romano, N E Horelik, B R Herman, A G Nelson, B Forget and K Smith, OpenMC: a state-of-the-art Monte Carlo code for research and development, *Ann. Nucl. Energy* **82** 90 (2015). doi:10.1016/j.anucene.2014.07.048

11 J R Tramm and A R Siegel, Immortal rays: rethinking random ray neutron transport on GPU architectures, *Parallel Comput.* **108** 102832 (2021). doi:10.1016/j.parco.2021.102832

12 K Hamada *et al*, Engineering design of cryoplant for ITER, in *Proc. 16th Int. Cryogenic Engineering Conf.* (Elsevier, 1997) p. 157. doi:10.1016/b978-008042688-4/50031-4

13 R Heller, W H Fietz, R Kienzler and R Lietzow, High temperature superconductor current leads for fusion machines, *Fusion Eng. Des.* **86** 1422 (2011). doi:10.1016/j.fusengdes.2010.12.077

14 S Varoutis and Chr Day, Numerical modeling of an ITER type cryopump, *Fusion Eng. Des.* **87** 1395 (2012). doi:10.1016/j.fusengdes.2012.03.023

15 W L Barr, R W Moir and G W Hamilton, Experimental results from a beam direct converter at 100 kV, *J. Fusion Energy* **2** 131 (1982). doi:10.1007/BF01054580

16 R F Post, The magnetic mirror approach to fusion, *Nucl. Fusion* **27** 1579 (1987). doi:10.1088/0029-5515/27/10/001

17 S Hahn *et al*, 45.5-tesla direct-current magnetic field generated with a high-temperature superconducting magnet, *Nature* **570** 496 (2019). doi:10.1038/s41586-019-1293-1

18 S Hahn, Y Kim, D K Park, K Kim, J P Voccio, J Bascu\ n\'an and Y Iwasa, No-insulation multi-width winding technique for high temperature superconducting magnet, *Appl. Phys. Lett.* **103** 173511 (2013). doi:10.1063/1.4826217

19 M Marchevsky, Quench detection and protection for high-temperature superconductor accelerator magnets, *Instruments* **5** 27 (2021). doi:10.3390/instruments5030027

20 E E Salazar *et al*, Fiber optic quench detection for large-scale HTS magnets demonstrated on VIPER cable during high-fidelity testing at the SULTAN facility, *Supercond. Sci. Technol.* **34** 035027 (2021). doi:10.1088/1361-6668/abdba8

21 L L Lao, H St John, R D Stambaugh, A G Kellman and W Pfeiffer, Reconstruction of current profile parameters and plasma shapes in tokamaks, *Nucl. Fusion* **25** 1611 (1985). doi:10.1088/0029-5515/25/11/007

22 N C Amorisco *et al*, FreeGSNKE: a Python-based dynamic free-boundary toroidal plasma equilibrium solver, *Phys. Plasmas* **31**

COLOPHON

How this document was made

The Kronos Fleet — Combined Editorial, 2026 is set in **Fraunces** (display), **Gelasio** (text), and **IBM Plex Mono** (data & equations), carried forward from the Kronos editorial design system.

The figures are rendered at 300 dpi from the deposited generator scripts; the document is composed as a single self-contained file with embedded fonts and imagery, paginated to US Letter, and rendered to PDF through a headless Chromium engine in matched light and dark editions.

Every headline quantity carries an evidence class; withdrawn and restated values are marked as such. Nothing herein is frozen beyond the founder-approved Tier-A set.

Explore it live — turn the interactive 3-D model, run the deposited solvers in the physics validator, and watch the companion film series.

LEGAL NOTICE

Notice, status, and distribution

Conceptual design & simulation study. This document reports a conceptual design and simulation study. It is not a construction commitment, a safety-analysis report, a regulatory filing, or an offer of securities. Forward-looking statements — schedules, costs, market sizes, and performance — are estimates subject to the limitations set out in the Simulations part and may change.

Numbers and their classes. Quantities are reported with evidence classes and case labels; modelled, assumed, and requirement-class values are identified as such and are not to be quoted without their labels.

Public edition. This edition carries the physics and design only; all financial, funding, and defense-commercial content has been removed for public distribution. The scientific text corresponds to the arXiv and journal submissions.

THE 2026 KRONOS SERIES

One programme, many papers

This editorial is one paper in the Kronos 2026 series — a real fusion company's complete, reproducible physics record for a spherical-tokamak breeder and its low-neutron D–^{3}He tandem-mirror burners. Every headline number is a frozen anchor in the Physics De-Risking Register.

Explore the whole programme: the De-Risking Register, the interactive 3-D model, and the physics validator.

KRONOS FUSION ENERGY

Balance of Plant for a Compact Spherical-Tokamak Breeder: Heat Rejection, Cryoplant Load-Balancing, and Vacuum Scheduling for the 16.84 T Cold Mass

A real fusion company building real machines. Explore the science, live.

Zenodo · doi:10.5281/zenodo.22645901

Read on kronosfusionenergy.com

The Physics De-Risking Register